Atmospheric Research 182 (2016) 335–345

Contents lists available at ScienceDirect

Atmospheric Research

journal homepage: www.elsevier.com/locate/atmosres

Response of rainfall to land surface properties under weak wind shear conditions

Yuya Baba

Application Laboratory, Japan Agency for Marine-Earth Science and Technology, 3173-25 Showa-machi, Kanazawa-ku, Yokohama 236-0001, Japan

ARTICLE INFO

Article history:
Received 1 March 2016
Received in revised form 14 July 2016
Accepted 11 August 2016
Available online 16 August 2016

Keywords:
Rainfall
Land surface properties
Convective structure

ABSTRACT

Responses of rainfall trends to land surface properties (roughness length and sensible heat flux) under weak wind shear conditions were investigated by numerical simulation and idealized experiments. The results show that total amount, spatial pattern and intensity of rainfall were highly affected by the difference in sensible heat flux rather than the difference in roughness length. The initiation time for occurrence of rainfall became more delayed and the rainfall intensified as the given sensible heat flux decreased. A smaller sensible heat flux and a larger roughness length increased the convective available potential energy before the rainfall occurrence, resulting in stronger initial convection. The initiation processes affected the resulting convective structure, such that initial latent heat release occurred and remained downstream, leading to a widely spread convective structure above the cold pool. Spread and connected convection magnified the upright structure, thereby causing release of much more latent heat for ice water species and thus stronger rainfall intensity.

1. Introduction

Rainfall trends change according to land surface properties such as roughness length, sensible (and latent) heat flux when the topographical gradient is small, especially over in-land urban area. Observational studies have indicated that the existence of urban area influences rainfall trends (e.g., Jauregui and Romales, 1996; Bornstein and Lin, 2000; Shephered et al., 2002; Diem and Mote, 2005). Results of numerical studies also suggest that urbanization can cause rainfall to increase (e.g., Thielen et al., 2000; Baik et al., 2001; Rozoff et al., 2003; Han and Baik, 2008; Miao et al., 2011). However, some studies have shown the contrary, that is, urbanization does not cause an increase in rainfall, thus, there are still uncertainties regarding the effect of surface properties on rainfall patterns (Dabberdt et al., 2000; Kanae et al., 2004).

Variation of land surface properties affects rainfall trends through the surface fluxes, with their effects tending to vary with the conditions. Numerical simulations have revealed the sensitivity of rainfall to factors related to land surface properties. Thielen et al. (2000) noted that sensible heat flux (SHF) has a significant impact on rainfall change. Han and Baik (2008) investigated initiation of convection due to thermal forcing mimicking urban heat island effect, and simulated different response of rainfall to the different forcing. Miao et al. (2011) reported that rainfall increase mainly derives from SHF and latent heat flux rather than from momentum flux. These studies indicate that thermal forcing from the land surface is more important for generating convection than the momentum flux. However, an effect of nonlinear interaction between thermal and momentum fluxes on rainfall has been recognized (Rozoff et al., 2003), thus the effect of momentum flux (which derives from roughness of land surface) on rainfall cannot be negligible.

Another important factor affecting rainfall trends that is related to surface flux is the wind profile of atmospheric condition. Differences in wind shear are known to alter convective activity and structure, resulting in different rainfall trends (e.g., Weisman et al., 1988; Fovell and Ogura, 1989; Ferrier et al., 1996; Weisman and Rotunno, 2004). Findings of studies on the sensitivity of convection to wind shear indicate that wind profile can affect rainfall trends induced by land surface properties. In particular, weak wind shear or weak wind speed has been observed in events of strong rainfall intensity (e.g., Bornstein and Lin, 2000; Kim et al., 2012). Therefore, the mechanism of convection formation under such condition and the sensitivity to the land surface properties need further study to understand in-land heavy rainfall.

The purpose of this study is to examine the response of rainfall trends to land surface properties under weak wind shear conditions using numerical simulation and idealized experiments. The analysis

E-mail address: babay@jamstec.go.jp (Y. Baba).

http://dx.doi.org/10.1016/j.atmosres.2016.08.010

focuses on detailed initiation and transition processes of convection in terms of rainfall intensity induced by land surface properties. For simplicity, orography is not considered; thus, the orographic effect on rainfall is not discussed in this paper. In order to simplify the effect of land surface properties including urban area on rainfall, the model uses prescribed roughness lengths and SHFs. In Section 2, details of numerical experiments are described. In Section 3, an overview of rainfall trends is presented, and the initiation of rainfall is investigated. The convective structure of subsequent convection and its transition process are then discussed. Section 4 gives a summary and provides the conclusions of the study.

2. Numerical experiments

In this study, the response of rainfall is investigated by using presumed land surface properties. The surface roughness length (SRL) condition is given by using a Gaussian function,

$$z_0(x) = z_m e^{-x^2/a^2} + z_o \tag{1}$$

where $z_0(x)$ is the SRL for momentum surface flux; it is a function of x, the horizontal coordinate, z_m is the maximum SRL, and a (= 25 km) is the half width of the region of increased roughness length. The value of a approximates urban width of 50 km (e.g., Rozoff et al., 2003; Miao et al., 2011). z_o (= 1×10^{-2} m) is the background roughness length. The sensible heat flux (SHF) condition is also described by a similar Gaussian function,

$$F = Q_H e^{-x^2/a^2}, \tag{2}$$

where Q_H is the constant SHF. Here, the latent heat flux is set to zero, since the effect is known to have less significance on rainfall change than SHF when the atmospheric condition is moist (Thielen et al., 2000). Some studies showed that the existence of urban results in decreasing latent heat flux and modifying location of rainfall (e.g., Rozoff et al., 2003; Miao et al., 2011), however, the effect is considered not to contribute to rainfall intensity directly and thus is omitted for simplicity.

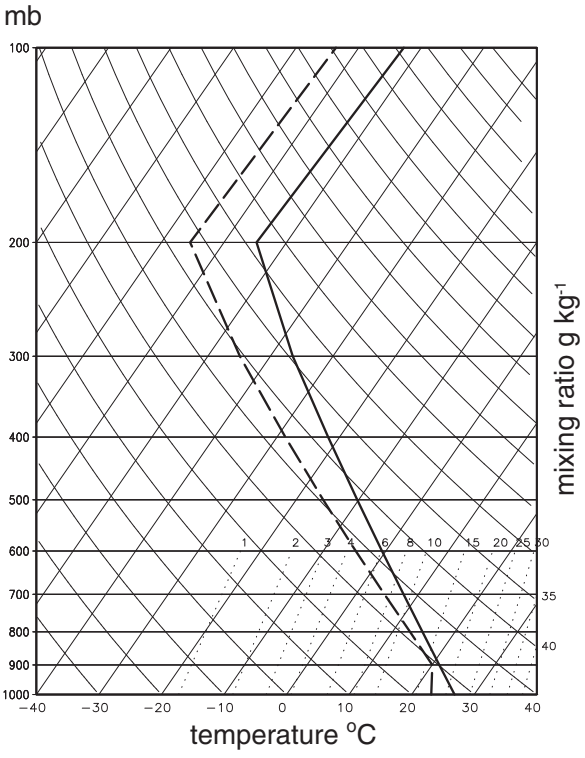

Fig. 1. Skew-T lop-P plot of the initial meteorological condition. Solid and dashed lines represent temperature and dew point temperature, respectively.

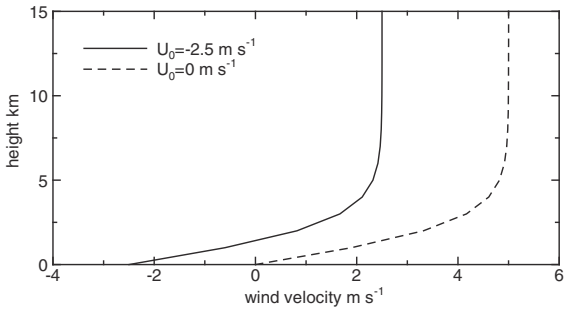

Fig. 2. Vertical profile of the initial wind velocity. Solid line: initial wind profile in the present study; dashed line: original wind profile.

The present experimental setup for the meteorological condition is based on a study by Weisman and Klemp (1982). The skew-T log-P plot of this condition is shown in Fig. 1. In their study, low-level maximum water vapor mixing ratio q_{v0} is limited to a certain value to represent boundary layer. This value is set to 18 g kg^{-1} in the present study in order to initiate convection within the duration of time integration (the resulting convective available potential energy (CAPE) is approximately 3000 J kg^{-1}). The horizontal westerly wind velocity U from the study of Weisman and Klemp (1982) is modified as follows:

$$U(z) = U_s \tanh\left(\frac{z}{z_s}\right) + U_0, \tag{3}$$

where U_s is the maximum wind velocity (set to 5 m s^{-1}), U_0 is the background wind velocity (set to −2.5 m s^{-1}), z is the vertical coordinate, and z_s = 2.5 km. The present wind profile is set to mimic the typical vertical wind profile of weak-shear-wind profile obtained from observation, the wind direction is skewed between 2.5 km height and the ground surface (e.g., Houston and Wilhelmson, 2011; Kim et al., 2012) (Fig. 2).

The values of parameters considered in the present study are summarized in Table 1. The SRL and SHF are varied to examine their effect on the rainfall trends. Values of z_m in Table 1 (ranged from 10 to 20 m) are adopted from the study of Nakayama et al. (2011), and values of Q_H (ranged from 100 to 400 W m^{-2}) are based on observational values (Grimmond and Oke, 2002).

An atmospheric model (Baba and Takahashi, 2014) is used with different numerical setup in the present study. For simplicity, a two-dimensional computational domain is utilized. The maximum domain height is 20 km with non-uniform vertical 46 layers and the horizontal size is 2000 km at 2 km grid spacing. Here, a resolution lower than that used by Baba and Takahashi (2014) is chosen because the domain size and time integration need to be expanded. The horizontal sponge region is set such that open boundary conditions are applied to the horizontal direction. Rayleigh damping is applied to the upper 15 km region in order to avoid reflection of gravity waves. The top boundary condition is slip condition, and the surface flux for momentum based on the model of Louis (1979),

Table 1
Summary of parameters for the condition of land surface properties. z_m: maximum surface roughness length; Q_H: maximum sensible heat flux.

Parameter (unit)	Values
z_m (m)	10, 20
Q_H (W m^{-2})	100, 200, 300, 400

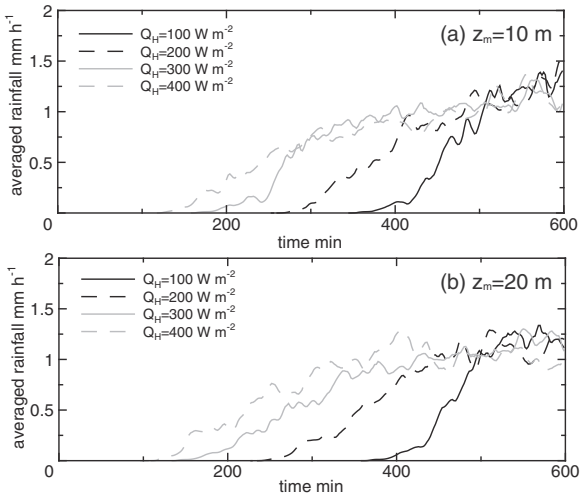

Fig. 3. Time variation of domain-averaged rainfall during 10h for all of the cases.

which depends on the roughness length, is assigned to the bottom boundary. Turbulence is modeled using a 1.5-order turbulent kinetic energy scheme of Deardorff (1980) which is commonly used with the present horizontal resolution. The warm anomaly was not set in the initial condition; thus, convection is spontaneously initiated by the effect of land surface properties. Although the increase in concentration of cloud condensation nuclei (CCN) is important to rainfall trends in in-land areas (e.g., Rosenfeld et al., 2007), the concentration is set to be constant ($100\,cm^{-3}$) nonetheless. Time step is 5 s, and time integration is performed for 10 h.

3. Results and discussion

3.1. Features of rainfall

The simulated features of rainfall are first investigated. Figure 3 shows the time variation of domain-averaged rainfall for all of the cases. The initial time for the occurrence of rainfall and the domain-averaged rainfall is found to depend on the land surface properties. The initial time of rainfall occurrence becomes earlier (later) as the imposed SHF becomes larger (smaller). The domain-averaged rainfall also slightly increases with the delay of the initiation of rainfall. Figure 3 also suggests that the qualitative trends of time variation of the domain-averaged rainfall are similar regardless of SRL.

A comparison of the total accumulated rainfall in each case with respect to different SRL and SHF conditions is presented in Fig. 4. Evidently, the amount of accumulated rainfall is proportional to the SHF. This proportionality is due to the strong dependence of the initiation of rainfall on the difference in SHF (Fig. 3) and to the longer period for the occurrence of rainfall as SHF increases. SHF impact is also apparently more significant than SRL impact. This result is consistent with

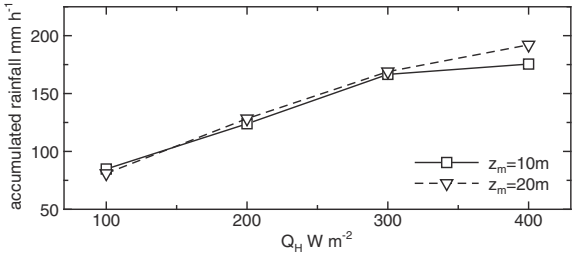

Fig. 4. Sensitivity of accumulated rainfall with respect to SRL and SHF.

the findings of previous studies that showed SHF has a more significant effect on change in rainfall amount compared with that of SRL (Miao et al., 2011; Thielen et al., 2000). Moreover, the accumulated rainfall in the cases with larger SRL is slightly larger compared with that of the cases with smaller SRL.

As with the trends of the total amount rainfall change, the rainfall intensity appears to change with the land surface properties. A comparison of rainfall intensities with respect to SHF is shown in Fig. 5. In general, the frequency of weaker rainfall decreases while that of stronger rainfall increases as the value of SHF decreases, regardless of the difference in SRL. The rainfall intensity is also sensitive to the change in SRL when the SHF is small; an increase in SRL generally results in an increase in rainfall intensity. However, such sensitivity is much smaller than the sensitivity to SHF.

Spatial patterns of rainfall during the time integration are compared in Figs. 6 (for $z_m = 10$ m) and 7 (for $z_m = 20$ m). In general, rainfall appears and moves eastward (toward downwind against the region of increased SRL and SHF) after convection occurs. The trends of increase in downwind rainfall are similar to those presented in preceding observational and numerical studies (e.g., Diem and Mote, 2005; Han and Baik, 2008). The time of initiation for rainfall depends on the SHF, as noted above. Delayed initiation tends to cause larger rainfall in the frontal region of rainfall moving eastward. The speeds of eastward movement of rainfall are almost identical (approximately $10\,m\,s^{-1}$) regardless of given parameters, except during the early stage of rainfall. This similarity may be due to the control of wind shear strength on the propagation speed of convective cells (Fovell and Ogura, 1989); the wind shear strengths for all cases are identical in the present study. At the early stage of rainfall initiation, the speed of eastward movement is slower than that during the later stage, showing deviation from the line of $10\,m\,s^{-1}$. The present rainfall pattern is also consistent with the results obtained by Thielen et al. (2000), namely, an increase in rainfall only near the urban region in case of smaller SHF and an increase in rainfall downstream in case of larger SHF. A finding that may not be explained in light of previous studies is an increase in rainfall intensity during delayed rainfall, which is obtained for smaller SHF. This trend is analyzed in detail in the following sections.

3.2. Initiation of convection

As presented above, the features of rainfall depend on the given parameters for land surface properties. (1) The difference in SRL has a small effect on nearly all changes in the rainfall, i.e., its amount, spatial pattern, and intensity. In contrast, the difference in SHF has a large impact on rainfall trends. (2) The initial time of rainfall occurrence becomes earlier (later) as the SHF increases (decreases), thus increasing (decreasing) the total accumulated amount of rainfall. (3) The frequency of strong rainfall increases while weak rainfall decreases as the SHF decreases.

Initialization of convection apparently has great effect on subsequent rainfall trends. Hence, the initiation process for convection is analyzed to reveal the mechanism behind the aforementioned effect. For this analysis, the initial time of rainfall occurrence, which can be a measure of the initiation time of convection, is defined (Table 2). Here, the initial time is the time when the maximum rainfall intensity exceeds $25\,mm\,h^{-1}$ which is a criterion used for identifying convective clouds (Xu, 1995). As presented above, the initial time generally becomes earlier when SHF increases, and also the time becomes slightly earlier when SRL increases, except for $Q_H = 100\,W\,m^{-2}$. In the following analysis, only the cases for which $Q_H = 200\,W\,m^{-2}$ (smaller SHF) and $400\,W\,m^{-2}$ (larger SHF) are analyzed for simplicity.

Before convection and rainfall occurrence, the flow field is modified by the land surface properties. Figure 8 displays vertical profiles of convective available potential energy (CAPE), and horizontal wind

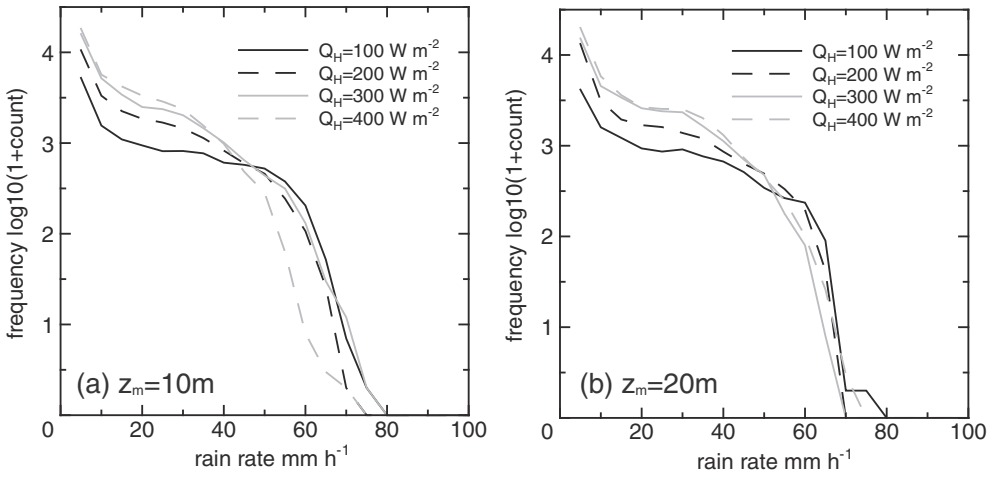

Fig. 5. Comparison of rainfall intensity for all of the cases.

velocity 1 h before rainfall. Since smaller SHF cannot cause immediate initiation of convection, the weak effect of land surface conditions on the lower atmosphere is apparent until convection occurs. This effect results in higher atmospheric instability; a smaller SHF indicates higher CAPE at lower altitude, as shown in Fig. 8 (a). The effect of SRL is different from that of SHF, since a larger SRL increases the CAPE near the surface. This difference is due to the tendency of a larger SRL to reduce surface wind velocity, which thus likely causes stagnation of heat and moisture above the region of larger SRL. This effect can be seen in Fig. 8 (b): a larger SRL reduces the wind velocity more than a smaller SRL does.

The vertical structure of subsequent convection formed depending on the existing atmospheric conditions. Figure 9 shows a comparison of vertical distributions of the cold pool and wind profile

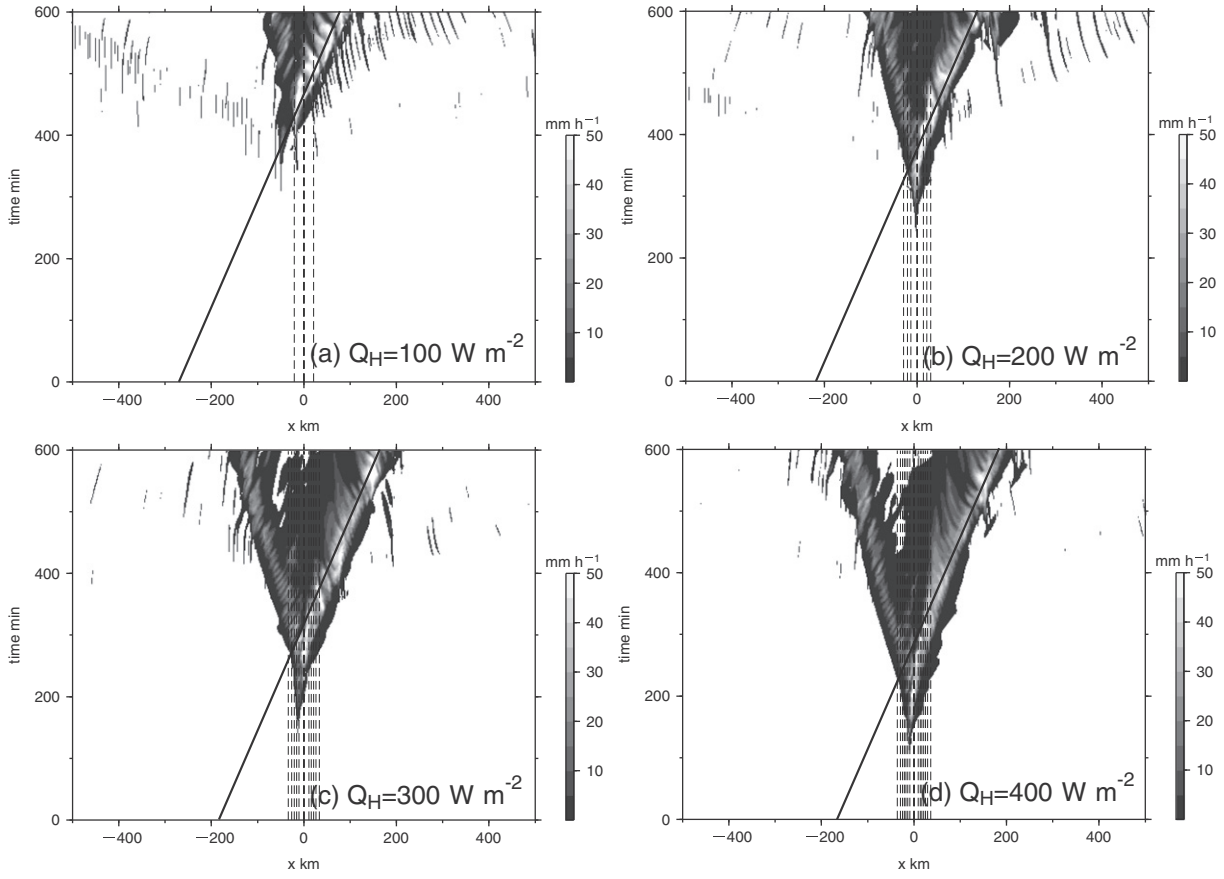

Fig. 6. Hovmöller diagrams of 10 h of rainfall for cases in which $z_m = 10$ m, showing rainfall larger than 0.01 mm h^{-1}. Dashed contour lines indicate SHF with interval of 50 W m^{-2}. Superimposed thin black lines representing 10 m s^{-1} speed of eastward movement are indicated for reference.

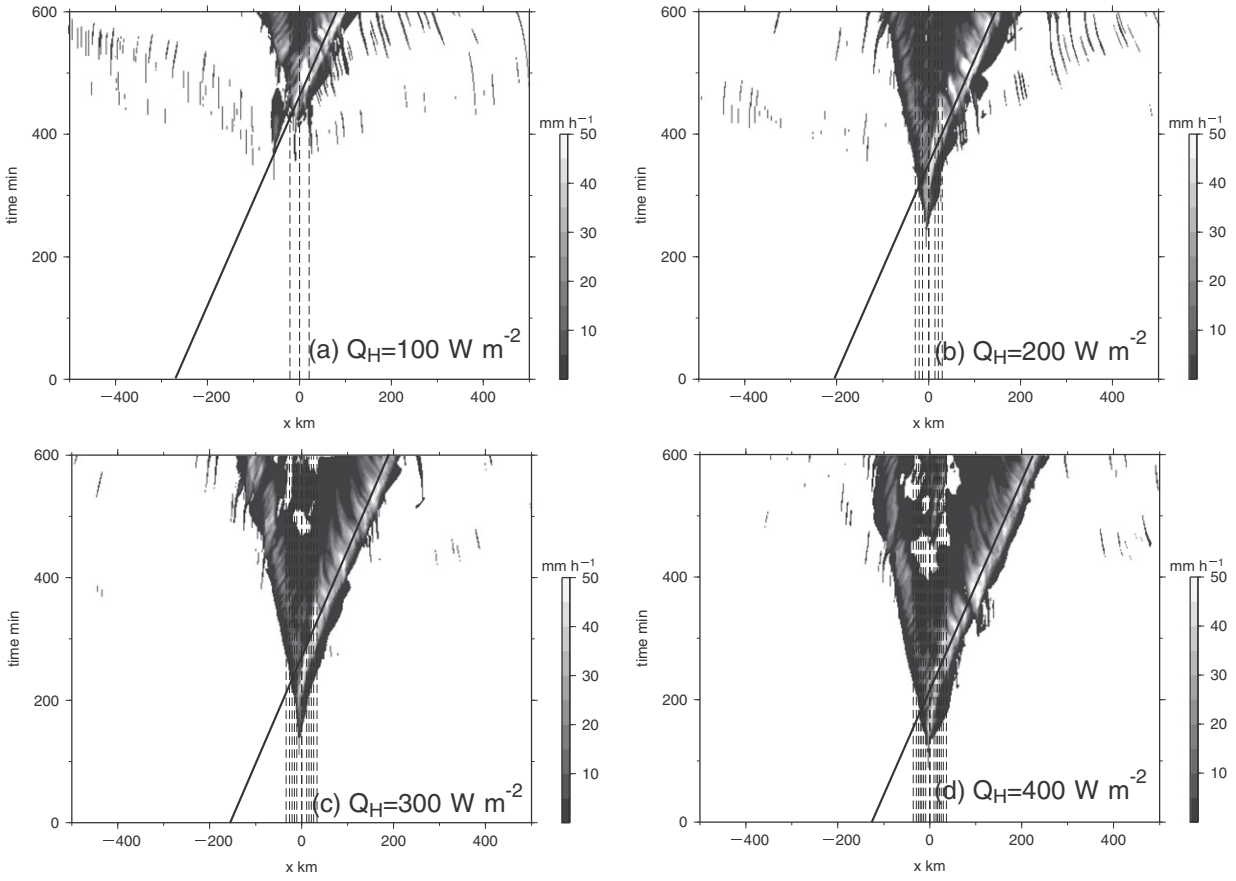

Fig. 7. Hovmöller diagrams of 10 h of rainfall for cases in which $z_m = 20$ m, showing rainfall larger than 0.01 mm h^{-1}. Dashed contour lines indicate SHF with interval of 50 W m^{-2}. Superimposed thin black lines representing 10 m s^{-1} speed of eastward movement are indicated for reference.

1 h after rainfall occurrence. In all of the cases, the upper convergent wind, and lower easterly wind emerged. Below the convergence region of these winds, air that is colder than the environmental air deriving from the downdraft of initial convection emerges. According to the CAPE profiles presented above, a more upright convective structure forms when the given SHF is small, since a higher CAPE leads to stronger initial convection. This trend is indeed apparent in Fig. 9; structures in Fig. 9 (a) and (c) are upright and horizontally narrower than those in Fig. 9 (b) and (d).

The initiation of convection is further analyzed by using vertical distributions of the moisture fluxes (Fig. 10). 1 h before the rainfall occurrence, the upper westerly incoming moisture flux is generally supplied to the convergence region where the uplifted air is present. Simultaneously, the lower easterly flux is supplied to the lower convergence region. Fig. 10 also suggests that moisture moving in a much more westerly direction is supplied into the upper convergence region when the SHF is small. This movement can lead to greater production of ice water species at higher altitude.

Table 2
Initial time of rainfall occurrence for all of the cases. Start times (in h) are identified by the time when maximum rainfall intensity exceeds 25 mm h^{-1}.

Q_H W m^{-2}	$z_m = 10$ m	$z_m = 20$ m
100	370 min (6.1 h)	380 min (6.3 h)
200	286 min (4.7 h)	256 min (4.2 h)
300	224 min (3.7 h)	156 min (2.6 h)
400	140 min (2.3 h)	134 min (2.2 h)

3.3. Convective structure

After initiation, subsequent convection forms, and the resulting structure controls rainfall trends. Figure 11 presents a comparison of vertical distributions of cold pool and wind velocity with rain mixing ratio during the last 2 h. The results show that the difference of land surface properties affects the convective structure, with the effects persisting for a certain period. When the assigned SHF is small, the updraft velocity is apparent only above the cold pool, and large amounts of rain accumulate downstream (against the direction of propagating convection, i.e., western region). When the assigned SHF is large, the updraft velocity is apparent not only above cold pool but also in the upstream region (eastern region), and large amounts of rain accumulate upstream. These trends indicate that smaller SHF tends to cause upright and downshear structure, whereas a large SHF results in a tilted and upshear structure (e.g., Ferrier et al., 1996).

The time evolution of cold pool depth and the intensity are compared in Fig. 12. The cold pool depth is defined as the height at which the negative buoyancy b exceeds −0.005 m s^{-2} (Tompkins, 2001). b is defined as

$$b = g\frac{\theta_v - \theta_{v,e}}{\theta_{v,e}}, \tag{4}$$

where g the gravitational acceleration, θ_v the virtual potential temperature, $\theta_{v,e}$ the environmental virtual potential temperature which

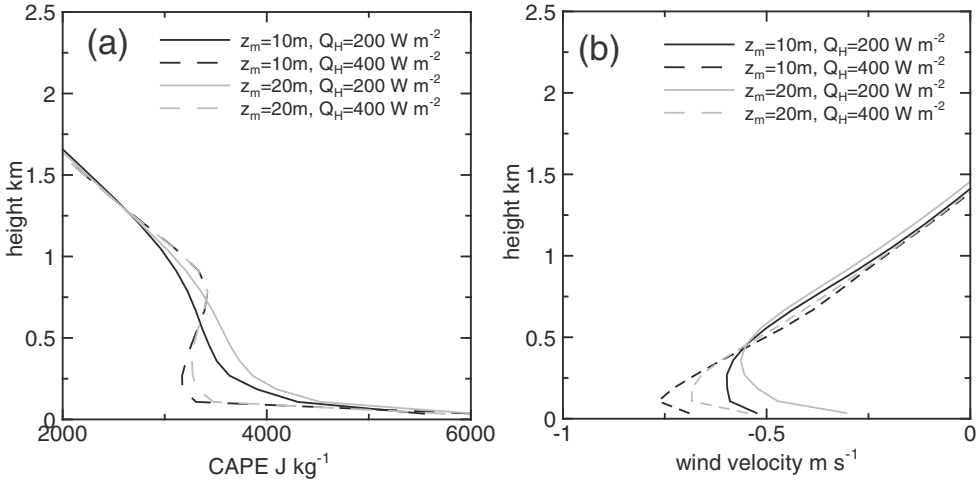

Fig. 8. Vertical profiles of (a) convective available potential energy (CAPE) and (b) horizontal wind velocity 1 h before rainfall occurrence. Vertical profiles were averaged between $x = -100$ to $x = 100$ km.

is set to the initial θ_v. The cold pool intensity B is defined in terms of b (e.g., Benjamin, 1968):

$$B^2 = 2\int_0^h (-b)dz, \tag{5}$$

where h is the cold pool depth, and z is the vertical coordinate. The simulated cold pool depth is approximately 2000 m which is comparable to that obtained by Houston and Wilhelmson (2011). The cold pool intensity is 20 m s^{-1}, which is similar to the intensity reported by Weisman and Rotunno (2004). Approximate values for cold pool depths and intensities are similar in all of the cases, but their trends are different. In the cases with smaller SHF, a deeper cold pool and stronger intensity initially form (as shown in Fig. 9), and the intensity remains strong for 3 h after the occurrence of strong rainfall. This result implies that the initial strength of the cold pool affects the formation of convection much more (even about after 3 h) when the assigned SHF is small.

The distribution of rain drop size changes depending on the difference in convective structure. Figure 13 presents vertical distributions of rain mixing ratio and rain drop size along with graupel mixing ratio. The rain drop size can be estimated from rain mixing ratio and its number concentration (e.g., Baba, 2015). The size increases as height decreases because of the growth of rain drops, which is generally caused by the collection of cloud condensate with rainfall (e.g., Morrison et al., 2009). An apparent difference between cases is that the region of large drops was more widely spread in the cases of smaller SHF compared with that in the cases of larger SHF. This difference indicates that larger rain size, which results in faster fall speed, tends to be frequent in the cases with small SHF. These conclusions are consistent with the above results showing that more frequent, stronger rainfall intensity appears in such cases. In addition

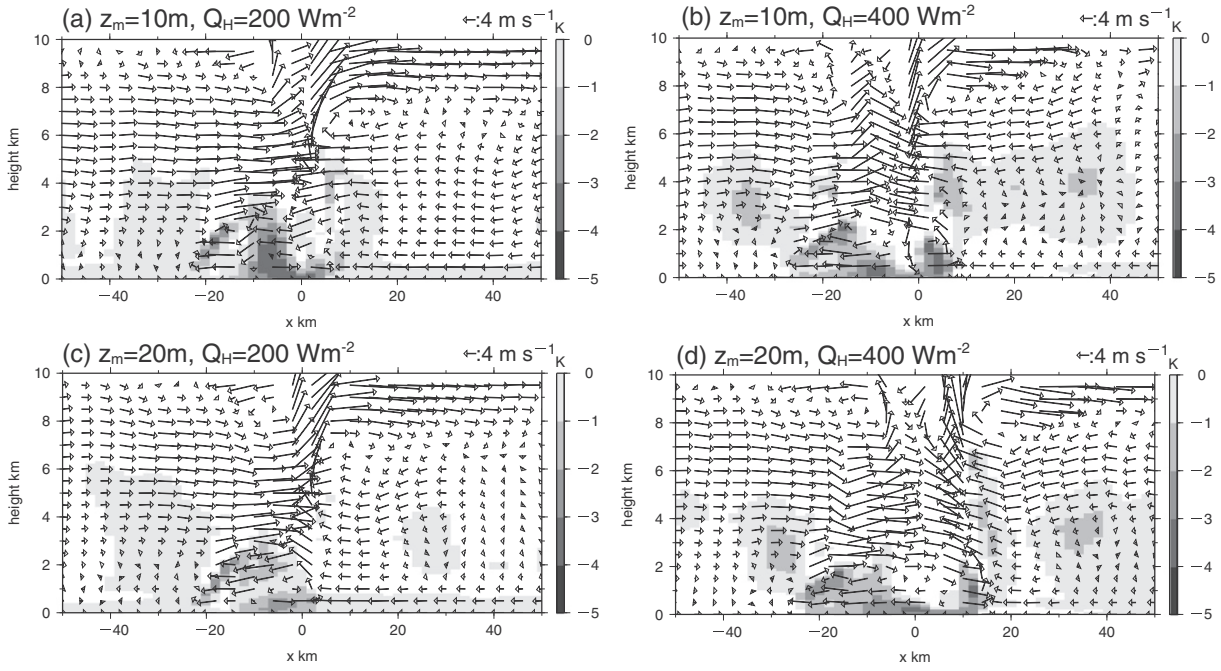

Fig. 9. Vertical distribution of cold pool as defined by the difference in equivalent potential temperature from the initial state (shaded areas) and wind velocity (vectors) 1 h after the rainfall occurrence. Each profile is time averaged for 1 h.

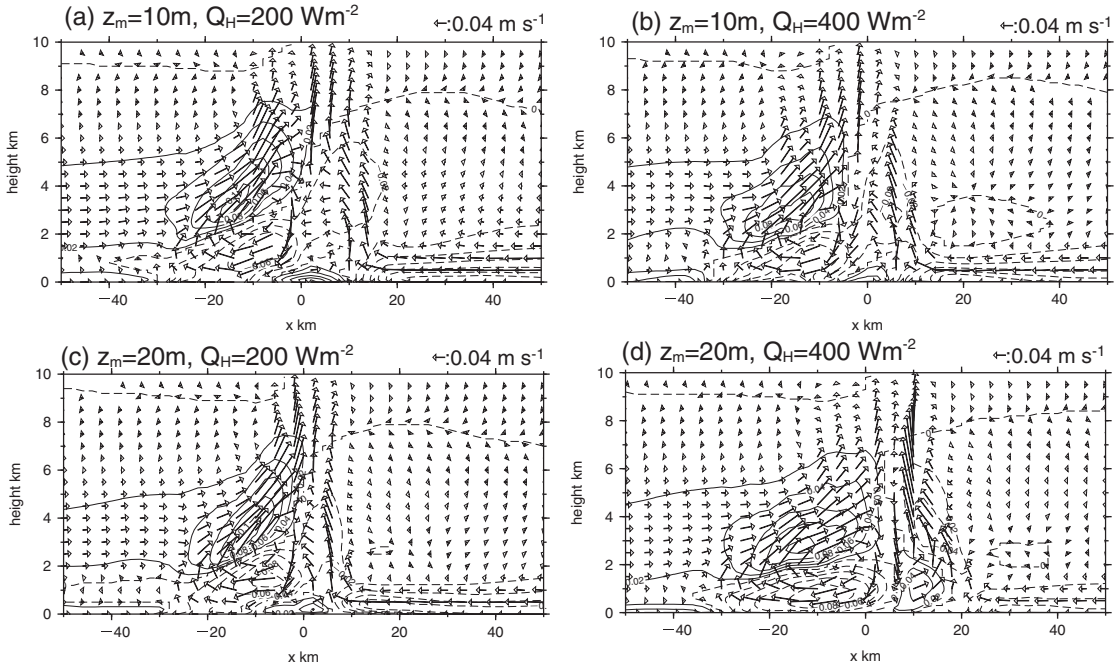

Fig. 10. Vertical distribution of moisture fluxes (vectors) 1h after the rainfall occurrence. Solid and dashed contour lines indicate westerly and easterly moisture fluxes, respectively. Each profile is time averaged for 1h.

to difference in the rain drop size distribution, there is also a difference in the graupel distributions. Larger graupel mixing ratio is apparent in the upper downstream region in the cases with smaller SHF and is apparent in the upper upstream region in the cases with larger SHF. These positions coincide with the regions with larger rain mixing ratio.

Large and heavy ice water species such as graupel produce rain through the melting process. Some studies have shown that an increase in graupel is closely related to an increase in rain because of the heavy mass of graupel. The increase results in stronger rainfall intensity (e.g., Wu et al., 2013; Baba and Takahashi, 2014). The above results suggest that the convective structure tends to be upright at smaller SHF, whereas it tends to be tilted at large SHF. When the structure is upright, transport of water species is in a more upward direction. This increased production is accompanied by the greater release of latent heat of ice deposition. Figure 14 shows the time variation of latent heat release derived from the production of ice water species. The variations clearly show that the difference in SHF mainly affects the latent heat release, with the gradient of increase persisting for up to 10 h.

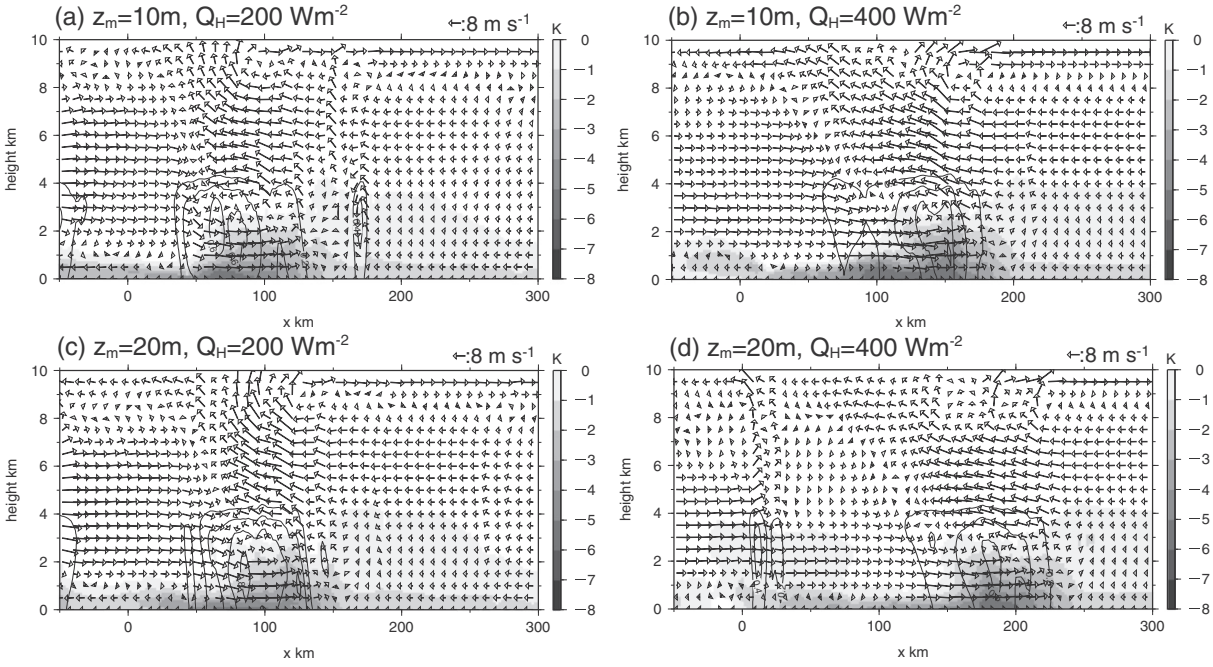

Fig. 11. Vertical distributions of cold pool (shaded areas represent differences in equivalent potential temperature from the initial state), wind velocity (vectors), and rain mixing ratio (contours; 0.2 g kg^{-1} interval) averaged during last 2 h. The vertical wind velocity is multiplied by 5.

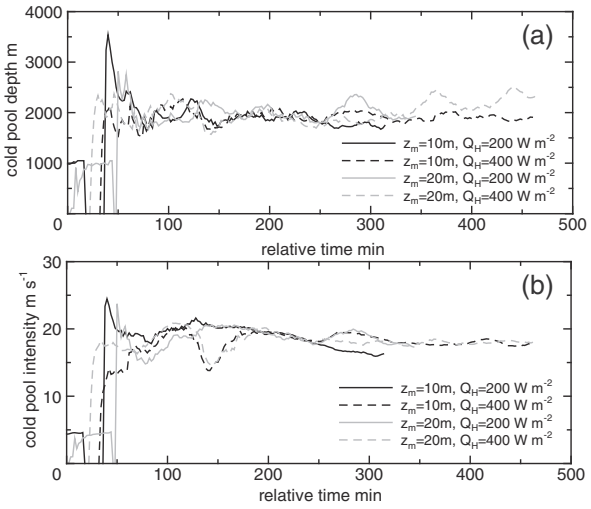

Fig. 12. Time evolution of (a) cold pool depth and (b) cold pool intensity. The time of evolution is the relative time for which the initial time is given in Table 2. The cold pool depths and intensities were conditionally averaged between columns in which cold pool was present.

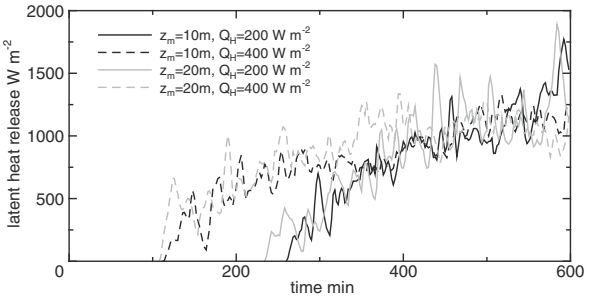

Fig. 14. Time variations of domain-averaged latent heat release for ice deposition. The value of latent heat release was domain-averaged and column-integrated.

They also suggest that a convective structure varies with the difference in the SHF throughout the development of convection. The sensitivity of latent heat release to SRL as the SRL slightly increases is also observable, but, as already noted, this sensitivity is relatively low.

Convective clouds produce large ice water species because they have large updraft velocity and can transport moisture toward higher altitude. Analysis of latent heat release within convective clouds as identified through the method of Xu (1995), shows increases in the latent heat releases from liquid and ice water species, as convection develops (Fig. 15). The trends of latent heat release also show that the increase in the rate of small SHF case is larger than that of large SHF case. The trends are found to be common for latent heat releases of both liquid and ice water species. However, the profile of latent heat release between small and larger SHF conditions is similar for up to 2 h; thus, significant structural change can occur between 2 and 4 h. Upward moisture transport within convective clouds responds to latent heat release (Fig. 16). Vertical profiles of vertical moisture transport clearly show that smaller SHF causes larger upward moisture transport within convective clouds at the same relative time shown in Fig. 15. Therefore, increased production of liquid water species precedes the increased production of ice water species.

Transition of convective structure with not only latent heat release for ice water species but also that for liquid water species after the rainfall occurrence is therefore considered to be a key to understanding the different rainfall trends. Figure 17 shows a comparison of transitions of convective structure with latent heat release at the same relative time. Multiple convective cells appear above the cold pool at 2 h in both cases. However, the relative positions of the largest latent heat release are different. The position is downstream in the case of smaller SHF and is upstream in the case of larger SHF. This difference is due to the stronger initial convection arising from higher CAPE in the former cases, resulting in a persistent effect of initial convection. Simultaneously, in this structure, difference of cold pool (Fig. 12) is seen mainly in downstream region, where westerly

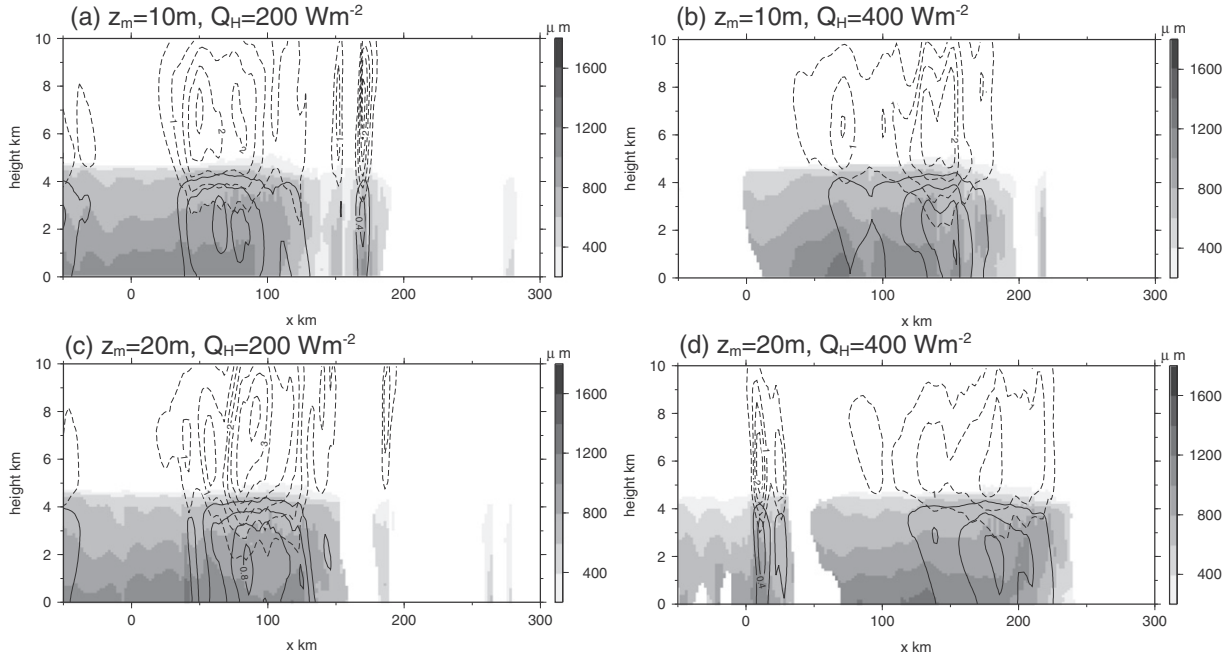

Fig. 13. Vertical distributions of rain drop size (shaded areas), rain mixing ratio (solid contour lines; 0.2 g kg^{-1} interval), and graupel mixing ratio (dashed contour lines; 0.5 g kg^{-1} interval). The distributions are time averaged during the last 2 h.

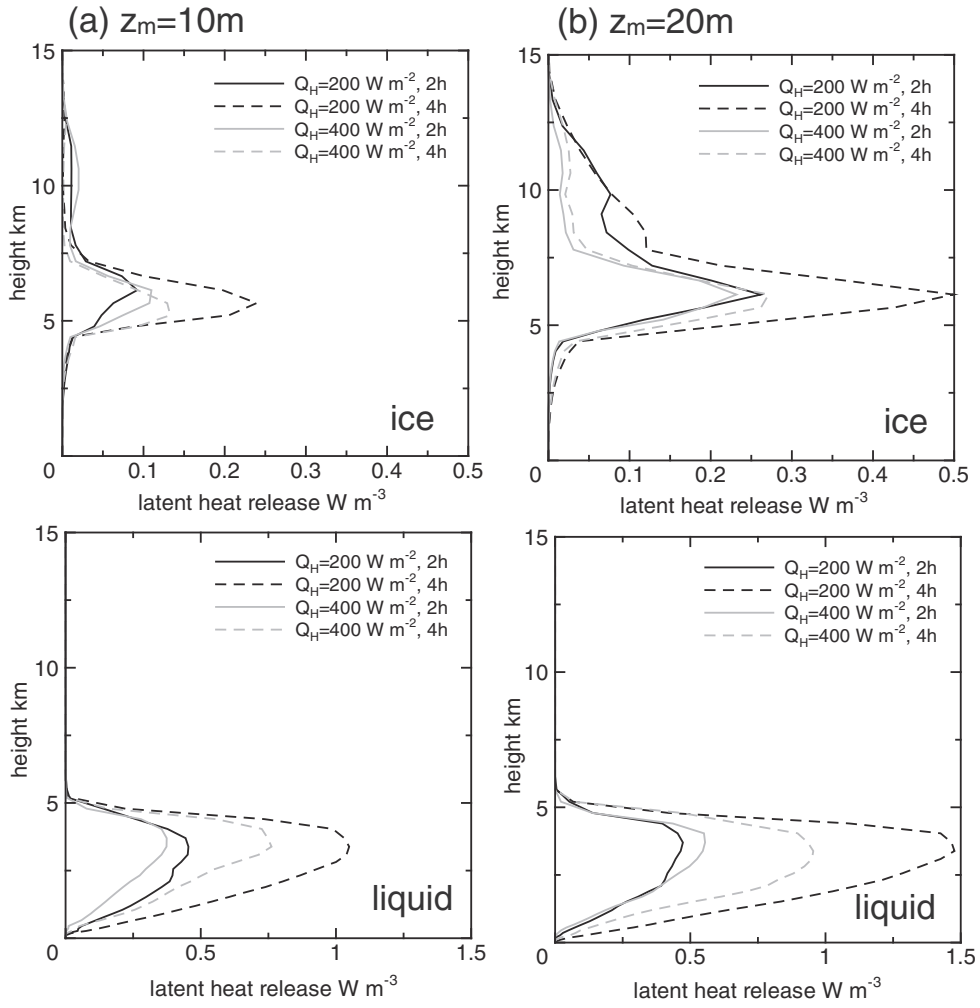

Fig. 15. Vertical profiles of latent heat release within convective clouds. The profiles are conditionally averaged by using cloudy columns. The time indicates the relative time after the occurrence of strong rainfall. 'liquid' and 'ice' indicate the latent heat releases that are derived from the productions of liquid and ice water species, respectively.

wind is uplifted into the convergence region. At 3 h after a significant change in the convective structure, the position of the large latent heat release shifts to upstream but large latent heat release remains downstream. Consequently, latent heat release above the cold pool is widely spread in the case of smaller SHF, as compared with that in the case with larger SHF. The widely spread, large latent heat release

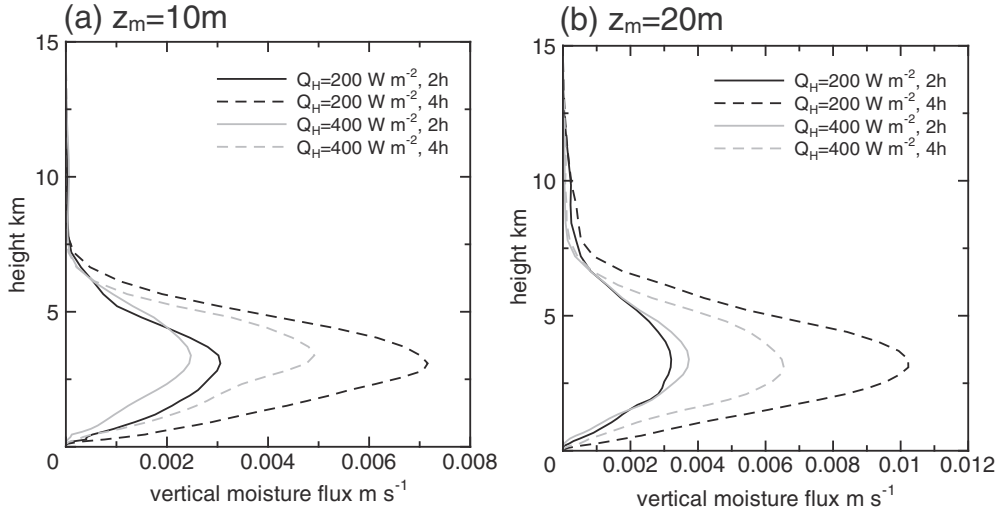

Fig. 16. Vertical profiles of vertical moisture flux within convective clouds. The profiles are conditionally averaged by using cloudy columns.

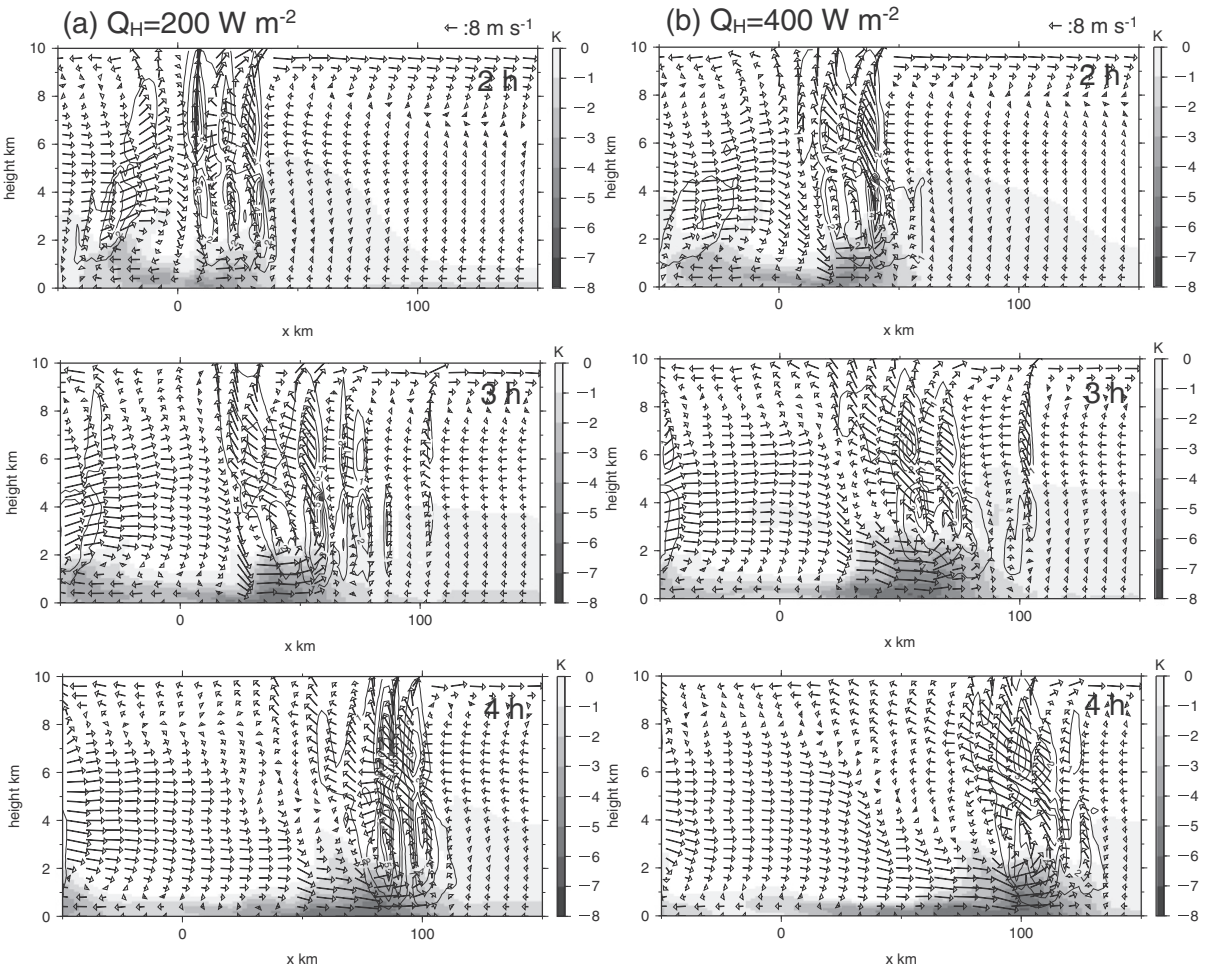

Fig. 17. Time variations of vertical profiles of wind velocity (vectors, vertical component is multiplied by 5), cold pool (shaded areas), and whole latent heat release (contours; 1.0 W m^{-3} interval) at 2, 3 and 4 h after occurrence of rainfall. Each profile is time averaged for 1 h. The cold pool is defined as done in Fig. 11. The maximum roughness length is set to $z_m = 20$ m (profiles of the cases for $z_m = 10$ m are omitted for simplicity, since they show similar trends).

magnifies the upright structure even after 4 h, with the remainder at the upper altitude. These trends of the transitions of convective structure suggest that the initial stronger convection influences the convective structure by linking each subsequent convection above the cold pool, leading to a more upright structure and larger rainfall intensity through production of more ice water species.

4. Summary and conclusion

The responses of rainfall to land surface properties under weak wind shear conditions were investigated by using numerical simulation and idealized experiments. In the investigation, the responses were mainly investigated in terms of rainfall intensity, using parameters of land surface properties which were chosen to be surface roughness length (SRL) and sensible heat flux (SHF) that have anomaly in their profiles to express urban area.

Rainfall spontaneously occurred in the downwind region against the region of increased SRL and SHF, with the given land surface properties and a wind profile in the absence of any initial force. The SRL had small impact on the rainfall amount and its intensity compared with the effect of SHF. The initial time for rainfall occurrence and the total amount of rainfall were mainly controlled by SHF: as the SHF increased (decreased), the initial time became earlier (later) and the total amount increased (decreased). Meanwhile, rainfall intensity increased and weak rainfall decreased with smaller imposed SHF.

The initial time for the occurrence of rainfall was defined, and details of the initiation process for all of the cases were investigated. At the same relative time with respect to rainfall occurrence, atmospheric instability as evidenced by the convective available potential energy (CAPE) increased with a smaller given SHF before convection occurred. Larger SRL increased the CAPE because the large SRL could cause stagnation of heat and moisture over the region with large SRL. Because of the difference in CAPE before occurrence of rainfall and convection, the initiation process for generating convection varied. A cold pool formed below the initial convection in all of the cases, but the resulting horizontal structure was narrower and deeper in the case of smaller SHF. Simultaneously, the moisture flux indicated the increased moisture supply toward the upper convergence region.

After the convection formed, the subsequent convective structure varied. Upon initiation of the initial convection by higher CAPE, a deeper and stronger cold pool intensity remained even 3 h after rainfall, and an upright structure remained during eastward propagation. In this structure, the rain drop size became larger and the distribution was widely spread, resulting in an increase in frequency of stronger rainfall intensity.

The strengthened rainfall intensity was derived from the increase in production of large ice water species, as suggested by the increase of latent heat release for ice deposition within convective clouds. The latent heat release was accompanied with that for liquid water species, indicating that total latent heat release increased in the upright structure. Analysis of the transition of the

convective structure revealed that initiation of convection by higher CAPE shifted the position of initial convection downstream above the cold pool and formed a widely spread convection with several convection currents linked to each other. In this structure, large latent heat release produced more ice water species; thus, the formation of such a convective structure triggered by higher CAPE might be a primary cause of the increased stronger rainfall intensity.

In conclusion, a delay in initiation of convection due to weak influences from land surface properties increases the CAPE before convection. The effect leads to downshear and an upright convective structure that can cause stronger rainfall intensity within a narrow region. The present mechanism for rainfall intensification may occur under similar atmospheric condition with more complicated urban region, since the properties of SRL and SHF for urban region are based on observational values. There might be possible effects of unresolved small scale structure and spatial variation of urban region on rainfall intensification, thus they should be discussed in future study. It also should be noted that the present mechanism for rainfall intensification appears only when the weak wind shear is maintained without being disturbed by change of atmospheric condition until strong convection occurs, thus the situation for rainfall intensification is limited. Finally, although the present study examined the response of rainfall to the land surface properties, further studies using three-dimensional models are necessary for a more comprehensive understanding of the response; the present study employed only a two-dimensional model.

Acknowledgments

This work was supported by the Japan Society of the Promotion of Science, Grant-in-Aid for Young Scientists (B), grant number 26820251.

References

Baba, Y., 2015. Sensitivity of the atmospheric energy budget to two-moment representation of cloud microphysics in idealized simulations of convective radiative quasi-equilibrium. Q. J. R. Meteorol. Soc. 141, 114–127. http://dx.doi.org/10.1002/qj.2342.

Baba, Y., Takahashi, K., 2014. Dependency of stratiform precipitation on a two-moment cloud microphysical scheme in mid-latitude squall line. Atmos. Res. 138, 394–413. http://dx.doi.org/10.1016/j.atmosres.2013.12.009.

Baik, J. J., Kim, Y. H., Chun, H. Y., 2001. Dry and moist convection forced by an urban heat islands. J. Appl. Meteorol. 40, 1462–1475. http://dx.doi.org/10.1175/1520-0450(2001)040%3C1462:DAMCFB%3E2.0.CO;2.

Benjamin, T. B., 1968. Gravity currents and related phenomena. J. Fluid Mech. 31, 209–248. http://dx.doi.org/10.1017/S0022112068000133.

Bornstein, R., Lin, Q., 2000. Urban heat islands and summertime convective thunderstorms in Atlanta: three case studies. Atmos. Environ. 34, 507–516. http://dx.doi.org/10.1016/S1352-2310(99)00374-X.

Dabberdt, W. F., Hales, J., Zubrick, S., Crook, A., Krajewski, W., Doran, J. C., Mueller, C., King, C., Keener, R. N., Bornstein, R., Rodenhuis, D., Kocin, P., Rossetti, M. A., Sharrocks, F., Stanley, E. M., Sr, 2000. Forecast issues in the urban zone: report of the 10th Prospectus Development Team of the U.S. Weather Research Program. Bull. Amer. Meteorol. Soc. 81, 2047–2064. http://dx.doi.org/10.1175/1520-0477(2000)081%3C2047:FIITUZ%3E2.3.CO;2.

Deardorff, J. W., 1980. Stratocumulus-capped mixed layers derived from a three-dimensional model. Bound.-Layer Meteorol. 18, 495–527. http://dx.doi.org/10.1007/BF00119502.

Diem, J. E., Mote, T. L., 2005. Interepochal changes in summer precipitation in the southeastern United Sates: Evidence of possible urban effects near Atlanta, Georgia. J. Appl. Meteorol. 44, 717–730. http://dx.doi.org/10.1175/JAM2221.1.

Ferrier, B. S., Simpson, J., Tao, W. K., 1996. Factors responsible for precipitation efficiencies in midlatitude and tropical squall line simulations. Mon. Weather Rev. 124, 2100–2125. http://dx.doi.org/10.1175/1520-0493(1996)124%3C2100:FRFPEI%3E2.0.CO;2.

Fovell, R. G., Ogura, Y., 1989. Effect of vertical wind shear on numerically simulated multicell storm structure. J. Atmos. Sci. 46, 3144–3176. http://dx.doi.org/10.1175/1520-0469(1989)046%3C3144:EOVWSO%3E2.0.CO;2.

Grimmond, C. S. B., Oke, T. R., 2002. Turbulent heat fluxes in urban areas: observations and a local-scale urban meteorological parameterization scheme (LUMPS). J. Appl. Meteorol. 41, 792–810. http://dx.doi.org/10.1175/1520-0450(2002)041%3C0792:THFIUA%3E2.0.CO;2.

Han, J. Y., Baik, J. J., 2008. A theoretical and numerical study of urban heat island-induced circulation and convection. J. Atmos. Sci. 65, 1859–1877. http://dx.doi.org/10.1175/2007JAS2326.1.

Houston, A. L., Wilhelmson, R. B., 2011. The dependence of storm longevity on the pattern of deep convection initiation in a low-shear environment. Mon. Weather Rev. 139, 3125–3138. http://dx.doi.org/10.1175/MWR-D-10-05036.1.

Jauregui, E., Romales, E., 1996. Urban effects on convective precipitation in Mexico City. Atmos. Environ. 30, 3383–3389. http://dx.doi.org/10.1016/1352-2310(96)00041-6.

Kanae, S., Oki, T., Kashida, A., 2004. Changes in hourly heavy precipitation at Tokyo from 1890 to 1999. J. Meteorol. Soc. Jpn. 82, 241–247. http://dx.doi.org/10.2151/jmsj.82.241.

Kim, D. S., Maki, M., Shimizu, S., Lee, D. I., 2012. X-band dual-polarization radar observations of precipitation core development and structure in a multi-cellular storm over Zoshigaya, Japan, on August 5, 2008. J. Meteorol. Soc. Jpn. 90, 701–719. http://dx.doi.org/10.2151/jmsj.2012-509.

Louis, J. F., 1979. A parametric model of vertical eddy fluxes in the atmosphere. Bound.-Layer Meteorol. 17, 187–202. http://dx.doi.org/10.1007/BF00117978.

Miao, S., Chen, F., Li, Q., Fan, S., 2011. Impacts of urban processes and urbanization on summer precipitation: a case study of heavy rainfall in Beijing on 1 August 2006. J. Appl. Meteorol. Clim. 50, 806–825. http://dx.doi.org/10.1175/2010JAMC2513.1.

Morrison, H., Thompson, G., Tatarskii, V., 2009. Impact of cloud microphysics on the development of trailing stratiform precipitation in a simulated squall line: comparison of one- and two-moment schemes. Mon. Weather Rev. 137, 991–1007. http://dx.doi.org/10.1175/2008MWR2556.1.

Nakayama, H., Takemi, T., Nagai, H., 2011. LES analysis of the aerodynamic surface properties for turbulent flows over building arrays with various geometries. J. Appl. Meteorol. Clim. 50, 1692–1712. http://dx.doi.org/10.1175/2011JAMC2567.1.

Rosenfeld, D. J., Dai, X., Yu, Z., Yao, X., Xu, X., Du, C., 2007. Inverse relations between amounts of air pollution and orographic precipitation. Science 315, 1396–1398. http://dx.doi.org/10.1126/science.1137949.

Rozoff, C. M., Cotton, W. R., Adegoke, J., 2003. Simulation of St. Louis, Missouri, land use impact on thunderstorms. J. Appl. Meteorol. 42, 716–738. http://dx.doi.org/10.1175/1520-0450(2003)042%3C0716:SOSLML%3E2.0.CO;2.

Shephered, J. M., Pierce, H., Negri, A. J., 2002. Rainfall modification by major urban areas: observations from spaceborne rain radar on the TRMM satellite. J. Appl. Meteorol. 41, 689–701. http://dx.doi.org/10.1175/1520-0450(2002)041%3C0689:RMBMUA%3E2.0.CO;2.

Thielen, J., Wobrok, W., Gadian, A., Mestayer, P. G., Creutin, J. D., 2000. The possible influence of urban surfaces on rainfall development: a sensitivity study in 2D in the meso-γ-scale. Atmos. Res. 15–39. http://dx.doi.org/10.1016/S0169-8095(00)00041-7.

Tompkins, A. M., 2001. Organization of tropical convection in low vertical wind shears: the role of cold pools. J. Atmos. Sci. 58, 1650–1672. http://dx.doi.org/10.1175/1520-0469(2001)058%3C1650:OOTCIL%3E2.0.CO;2.

Weisman, M. L., Klemp, J. B., 1982. The dependence of numerically simulated convective storms on vertical wind shear and buoyancy. Mon. Weather Rev. 110, 504–520. http://dx.doi.org/10.1175/1520-0493(1982)110%3C0504:TDONSC%3E2.0.CO;2.

Weisman, M. L., Klemp, J. B., Rotunno, R., 1988. Structure and evolution of numerically simulated squall lines. J. Atmos. Sci. 45, 1990–2013. http://dx.doi.org/10.1175/1520-0469(1988)045%3C1990:SAEONS%3E2.0.CO;2.

Weisman, M. L., Rotunno, R., 2004. A theory for strong long-live squall lines, revisited. J. Atmos. Sci. 61, 361–382. http://dx.doi.org/10.1175/1520-0469(2004)061%3C0361:ATFSLS%3E2.0.CO;2.

Wu, D., Dong, X., Xi, B., Feng, Z., Kennedy, A., Mullendore, G., Gilmore, M., Tao, W.-K., 2013. Impacts of microphysical scheme on convective and stratiform characteristics in two high precipitation squall line events. J. Geophys. Res. Atmos. 118, 119–135. http://dx.doi.org/10.1002/jgrd.50798.

Xu, K.-M., 1995. Partitioning mass, heat, and moisture budgets of explicitly simulated cumulus ensembles into convective and stratiform components. J. Atmos. Sci. 52, 551–573. http://dx.doi.org/10.1175/1520-0469(1995)052%3C0551:PMHAMB%3E2.0.CO;2.